# Decision Fusion for Urine Particle Classification in Multispectral Images

Charu Hans
Quantitative Imaging
Laboratory
University of Houston
Dept. of Computer Science
Houston, TX, U.S.A.
chans@cs.uh.edu

Fatima A. Merchant
University of Houston
Dept. of Engineering
Technology
Houston, TX, U.S.A.
fmerchan@central.uh.edu

Shishir K. Shah[*]
Quantitative Imaging
Laboratory
University of Houston
Dept. of Computer Science
Houston, TX, U.S.A.
shah@cs.uh.edu

## ABSTRACT

The microscopic analysis of the urinary sediment is important in making diagnoses for a variety of diseases, including urinary tract infection, urinary tract tumors, occult glomerulonephritis, and interstitial nephritis. A typical automated system acquires images of urinary sediment by employing a CCD camera, and then detects and recognizes the distinct particles automatically from these images. Automated recognition of these particles represents a significant challenge due to poor image resolution, strong variability of particle shape and size, and challenges associated with detection of particles in the presence of noisy backgrounds. In this paper, we present a novel method for urine particle classification based on the use of local descriptors coupled with regression based decision fusion. Specifically, DAISY descriptors have been used to capture the textural characteristics of each particle and subjected to dimensionality reduction across three linear subspaces to increase the diversity in decision making along with lowering the "curse of dimensionality". Classification in each subspace is based on computing a similarity score, which is then fused through support vector regression to obtain a final classification. The approach is applied to both brightfield and multispectral data to ascertain the benefits of multispectral imaging for urine analysis. Urine particles analyzed included crystals, casts and blood cells, and the results obtained show an average classification accuracy of 92.6% for 6 classes of urinary particles.

## 1. INTRODUCTION

Urinalysis (UA) is a vital laboratory test for evaluation of the renal and genitourinary systems. It allows physicians to diagnose asymptomatic patients. Once a diagnosis has been made, it enables them to follow the progression of illness and to recommend further treatment. The microscopic analysis

---

[*]Corresponding author

of the urinary sediment is critically important in making diagnoses for a variety of diseases, including urinary tract infection, urinary tract tumors, occult glomerulonephritis, and interstitial nephritis [23]. Current urinalysis techniques follows a two step strategy, the first step is to observe the characteristics of the urine such as color, pH, specific gravity etc., followed by microscopic analysis of particles in the urine sediment [18]. The microscopic examination of urine involves identification of physical composition of sediment color and morphological characterization of urine particles. Manual microscopic analysis relies on human operators who visually recognize the distinct particle types and provide a count measure for each. Therefore, manual analysis is time-consuming, labor-intensive, and difficult to standardize.

With recent advances in microscopy, it is appropriate to envision a fully automated urinalysis system that can eliminate the costs and errors associated with manual procedures. A typical automated system acquires images of urinary sediment by employing a CCD camera, and then detects and recognizes the distinct particles automatically from these images [4]. Various types of particles that need to be recognized include: 1) epithelial cells; 2) crystals (triple phosphate, uric acid, calcium carbonate and oxalate); 3) red blood cells (nonglomerular, crenated and intact); 4) casts (hyaline, granular, red blood cell, white blood cell, waxy); 5) yeast; and 6) bacteria. Automated recognition of these particles represents a significant challenge due to poor image resolution, strong variability of particle shape and size, and challenges associated with detection of particles in the presence of noisy backgrounds [19]. Further, combined classification of crystals, casts and various other particles is a challenging problem to study.

In the design and development of an automated Urinalysis system, detection and classification of sediment particles are two critical issues related to image analysis. Many methods have been proposed for classifying particles in urinary sediment. In [17], the authors use a fuzzy neural network to recognize distinct particles. The features used for classification were computed from binarized images and comprised of particle size, shape, and a degree of shape deformation. Similarly, in [26], the authors used a neural network to classify white and red blood cells. In this case, the features used were size, change rate of the gray level value measured between the particle edge and the central area, and the change frequency within the central area. Mei-Li et al. [16] used length, height, area, perimeter, equivalent radius, Fourier

descriptor, and shape features to train a support vector machine (SVM) for classifying urine particles. Another approach leveraging global descriptors was proposed by Dahmen et al. [6], where Fourier-Mellin features were computed and their distribution for each particle type was modeled using a mixture of Gaussians. Using these models, they achieved a test error rate of ≈15% for classifying three different types of red blood cells based on gray-scale images with a resolution of $128 \times 128$ pixels. Ranzato et al. presented an automatic system to classify 12 object categories in urinary images [19]. Without any segmentation, the differential invariants of brightness at multiple scales were described by an average operator. With these invariant features, a classifier obtained from a mixture-of-Gaussian generative model achieved 93.2% accuracy. However, their dataset did not include crystals. The current status of crystal morphology modeling and prediction techniques further emphasizes the need for better urine classification methods.

More recently, multispectral microscopes capable of acquiring spectral images under transmitted illumination have been used in analyzing cells and tissues [20]. Spectral images are three dimensional cubes of data $I_{x,y}(\lambda)$ comprised of a series of 2D images, $I_{x,y}$, one for each wavelength. Each pixel location, $(x, y)$, contains a spectral signature, stored along the $\lambda$ axis, as is shown in figure 1. Studies have shown
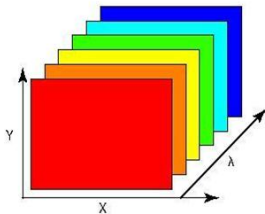


Figure 1: Spectral image represented as a stack of images, where each image corresponds to the image acquired at a specific wavelength.

that biological tissue exhibits unique spectra in transmission. By exploring the spectral differences in tissue pathology, many chemical and physical characteristics not revealed under traditional imaging systems can be realized and used to improve the analysis efforts [27].

In this paper, we propose a novel scheme for classification of urine particles using multispectral urine sediment images. First, we employ an adaptive thresholding approach to detect the location of particles. A connected component analysis is performed to identify distinct blobs and a region of interest (ROI) is identified by placing a bounding box around each blob centroid. Features are extracted from each ROI. We use DAISY descriptors to describe the characteristics of the detected regions. In order to reduce complexity and increase diversity in classification decisions, we project the descriptor to three lower dimensional subspaces based on Principal Component Analysis (PCA), Isometric Projection (ISO), and Neighborhood Preserving Embedding (NPE). Classification is based on a similarity metric to labeled examples in each subspace and the decisions are fused by using support vector regression (SVR). Figure 2 shows an overview of the proposed approach.

This paper is organized as follows: In section 2, we pro-
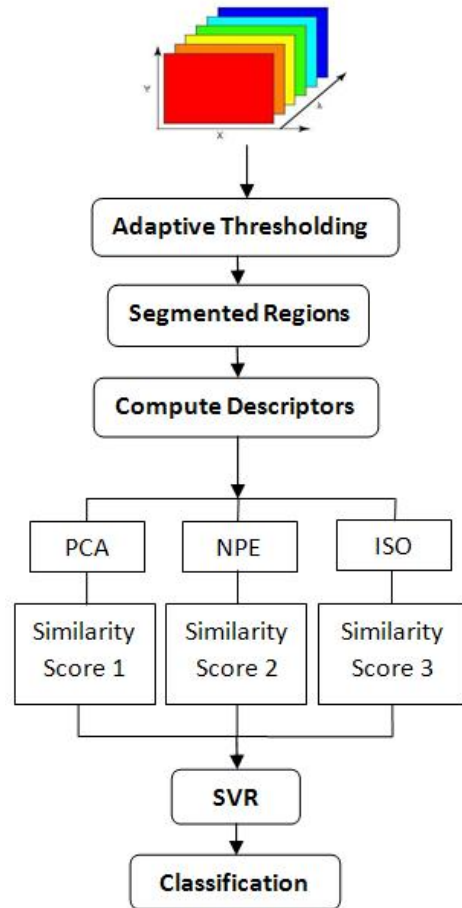


Figure 2: Overview of algorithm

vide details of our proposed approach, including the steps of segmentation, feature extraction, dimensionality reduction, similarity score, and feature fusion. Section 3 presents details of performed experiments and the obtained results. Finally, the paper is concluded in section 4.

## 2. METHODOLOGY

The ability to provide a discriminative representation of distinct urine particles while ensuring sufficient diversity is important in the development of a robust classification system. This poses a significant challenge due to variations in size, shape, and gray-level values, even for particles of the same type. For efficient local textural characterization of objects, point descriptors such as SIFT, SURF, and DAISY have been used extensively [14]. More specifically, DAISY has been shown to be a compact local descriptor providing improved discriminative representation for local image regions [24]. On the other hand, high-dimensional feature spaces are difficult to analyze. In order to reduce the complexity of the feature space, we project the computed features into three lower dimensional spaces. Each subspace provides increased diversity in representing a particle type. Particle are classified by computing a similarity score in each subspace and the final scores fused. Algorithm 1 shows an overview of the proposed approach. Rest of this section

presents details of each of the steps in our proposed method.

---

**Algorithm 1** Overview of the proposed algorithm.

---

**for** each image **do**

    1. Extract individual blobs from image using local adaptive thresholding and connected component analysis.

    2. Bounding box is placed around each blob centroid to delineate a region of interest.

    3. While scanning the region of interest along the wavelength axis (Figure 1), compute DAISY descriptor for each pixel.

    4. Subtract DAISY descriptor of corresponding pixels in the neighboring wavelengths.

    5. Arrange the difference of descriptors in one dimensional vector.

    6. Project the feature vector onto three subspaces based on PCA, ISO, and NPE.

    7. Compute similarity scores against representative features from each particle class.

    8. Fuse the scores obtained from each subspace using support vector regression.

**end for**

---

## 2.1 Segmentation

Imaging of urine particles is typically performed under transmitted illumination. This results in particles being darker than the background. This is true in case of both brightfield imaging as well as transmitted mode multispectral imaging. With the intent of identifying the location of different particles in an image, a multitude of thresholding approaches can be leveraged to separate dark objects against bright background, or vice versa. However, when the background has non-uniform illumination, a fixed (or global) threshold value can result in poor segmentation. To gain robustness to non-uniform intensity distributions, we employ local adaptive thresholding to identify different particles [9]. Morphological smoothing is performed on the resulting binary image followed by connected component analysis to identify the number of particles. The centroid of each particle provides an estimate of the spatial location. A bounding box is placed around each centroid to delineate the region of interest.

## 2.2 Feature Extraction

For each particle, we need to extract relevant features for discriminative representation. Local image descriptors have been widely used for addressing variety of problems in computer vision, from wide baseline matching and the recognition of specific objects to the recognition of object classes. They have been applied to image retrieval, image matching, texture recognition, scene classification, robot navigation, visual data mining, etc. [3, 25, 8]. In this work, we have opted to use DAISY descriptors to characterize each segmented region in the image.

*DAISY:.* DAISY was proposed by Tola et al. [24] with the objective of solving the dense stereo estimation problem, where the positions of the two cameras differ by a large amount. This descriptor is shown to outperform other approaches (e.g. SIFT, SURF and pixel differences) in exten-

sive experiments. Unlike SURF, which can also be computed efficiently at every pixel, it does not introduce artifacts that degrade the matching performance when used densely. Not unlike SIFT [15], a DAISY descriptor samples the image derivative in different directions. Eight different directions and three different scales are used. By sampling these fields at different points around the feature location, a descriptor of dimensionality 200 is obtained. Since the same fields are used for all image locations, a dense field of descriptors can be computed efficiently. Figure 3(a) and (b) displays the histogram of daisy descriptor, computed for a single pixel on a WBC and Triple Phosphate crystal across three different wavelength.

*DOD: Difference Of Descriptors:.* To extend the applicability of DAISY descriptors to spectral images, we propose to compute the difference of descriptors as features. This allows subtle differences among spectral data to be represented through point descriptors. Moreover, the differences are computed between neighboring wavelengths so as to capture local variations across the spectra. To do so, we compute the DAISY descriptor for each pixel across all wavelengths. For each spectral cube, we scan the cube along wavelength axis (refer to Figure 1), and for each neighboring spectral pixel along the wavelength axis, we subtract the corresponding descriptor measure. As a result, if a spectral image consists of 31 wavelengths, the resulting DOD descriptor would have a dimension of $30 \times 200$, where 200 is the length of the DAISY descriptor. Figure 3(c) and (d) shows the DOD of WBC and triple phosphate crystal for a single spectral pixel across 3 wavelengths. For a typical region of interest of size $25 \times 25$ pixels and the number of wavelengths in the spectral cube being 31, the resulting feature vector would be of a size equal to $1 \times (200 * 25 * 25 * 30)$. This imposes the "curse of dimensionality" and potentially penalizes classification. In general, high dimensional features tend to limit the performance of feature matching techniques in terms of speed and scalability. Furthermore, these descriptors have traditionally been carefully hand crafted by manually tuning many parameters. To overcome these issues, we use subspace projection methods to reduce the dimension of the DOD features.

In the case of brightfield microscopy, we have a single grayscale image and hence the dimensionality is not as large. For the same region of interest, the feature vector would be of size $1 \times (200 * 25 * 25)$, where instead of DOD features, the original DAISY descriptor is computed at each pixel.

## 2.3 Dimensionality Reduction

High-dimensional datasets present many mathematical challenges as well as some opportunities, and are bound to give rise to new theoretical developments [7]. Several researchers have addressed the problem of dimensionality reduction for feature descriptors. For example, Herbert et al. [1] proposed an approach (SURF) that combined the Hessian matrix-based measure for the detector and Haar-wavelet responses for the descriptor, resulting in a 64-dimensional feature representation. PCA-SIFT proposed in [12] reduced the dimensionality of the descriptor to 36 dimensions while providing comparative performance to the original SIFT. The key of PCA-SIFT is to apply the standard Principal Components Analysis technique to the gradient patches extracted around local features, therefore yielding a compact feature represen-
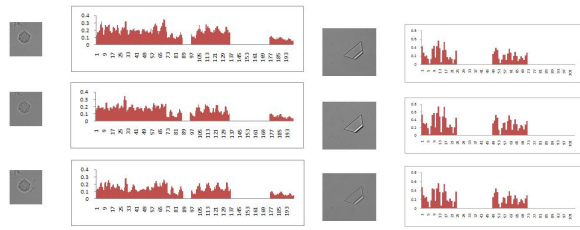
(a) Histogram of DAISY descriptor for same spectral pixel of WBC in different wavelength.

(b) Histogram of DAISY descriptor for same spectral pixel of triple phosphate crystal in different wavelength.
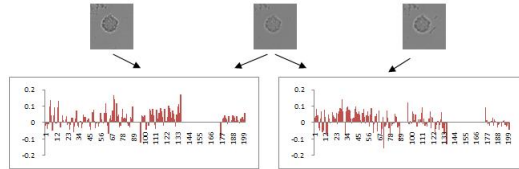


(c) Difference of Histogram of DAISY descriptor for same spectral pixel of WBC in different wavelength.
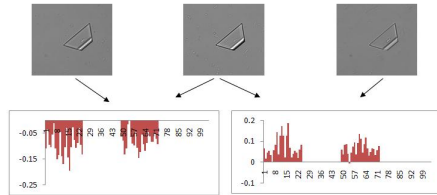


(d) Difference of Histogram of DAISY descriptor for same spectral pixel of triple phosphate crystal in different wavelength.

Figure 3: DAISY descriptor.

tation. In this paper, we reduce the DOD feature using three dimensionality reduction methods in order to obtain a more discriminant representation of the descriptors along with a possible increase in the diversity of classification decisions. Each projection provides a subspace within which a sample can be classified and the result eventually fused to obtain a combined result.

*Data Arrangement:.* Figure 4 shows our data arrangement for dimensionality reduction. Initially, a training dataset is established comprising of particles randomly sampled from all classes and the number of each particle type representative of the probability of occurrence of that class. For each particle, we raster scan the region of interest. In the case of spectral images, the scanning is done along the wavelength axis ((left)figure 4). DAISY descriptor is computed for each pixel and read into a row vector ((right)figure 4). Hence, a data matrix is generated from each image, where a row of the matrix represents one region of interest or particle. The data matrix is projected into a lower dimensional space to reduce the feature size using Principal component analysis [11], Neighborhood preserving embedding [10] and Isometric projection [2]. The feature vector is reduced to a 35 dimensional descriptor. The choice of the reduced number
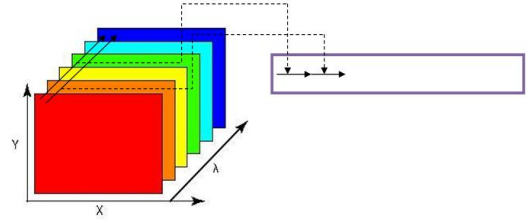


Figure 4: Shows the data arrangement for dimensionality reduction, row represents a data.

of dimensions was determined empirically.

## 2.4 Similarity Score

Within each projected subspace, one can compute similarity to representative (training) features in order to ascertain a class label for a test sample. Since there exists a large amount of variation within each particle class, it is difficult to generate a single representative feature for each class label. As a result, we choose to compute a similarity score that is established as a pairwise measure between a test sample and all the samples in the training dataset. Algorithm 2 summarizes the calculation of the similarity scores.

---
**Algorithm 2** Algorithm for similarity score computation.

**for** each training matrix row $i$ **do**
    1. Compute the similarity between test feature and all representative features using a similarity metric.
    2. Store the scores in a column vector at positions $((i)*size(training,1)+1:(i+1)*size(training,1),1)$ .
**end for**

---

We use the cosine distance metric as the function that measures the similarity scores for each test sample. Let $U$ and $V$ be two feature vectors. Say, $U = (u_1, u_2, ....., u_n)$ and $V = (v_1, v_2, ......, v_n)$, then

$$cos(U,V) = (U.V)/ \|U\| \|V\| \qquad (1)$$

A similarity score is computed independently in each of the projected spaces.

## 2.5 Support Vector Regression

The final step in establishing a class label for each particle is to combine the similarity scores computed in each projected space. Many approaches for combining local decisions have been proposed in the past few years [13], many of which assume independence of individual decisions. An alternative approach we have considered in this paper is one based on regression analysis that allows modeling of values of a dependent variable from one or more independent variables. Support Vector Machines, a popular mechanism for classification purposes can also be used for regression purposes. The basic ideas of nonlinear-support vector regression are as follows: Consider the training sample $S = ((x_1, y_1), ((x_2, y_2), ....., ((x_l, y_l))), S \subseteq (x \times y)^l, x \subseteq R^d, y \subseteq R$. In $\epsilon$-SV regression, the goal is to find a function $f(x)$ that has at most $\epsilon$ deviation from the actually obtained targets $Y_i$ for all the training data. The regressor must not only fit the given data well, but also makes minimal errors in predicting the values at any other arbitrary point in $R^d$.

Nonlinear regression is accomplished by fitting a linear regressor in a higher dimensional feature space. A nonlinear transformation $\phi$ is used to transform data points from the input space of dimension $D$ into a feature space having a higher dimension $L$. The nonlinear mapping is denoted by

$$\phi : R^d \to R^l \qquad (2)$$

In the feature space, the original non-linear function becomes a linear function $f(x)$.

$$f(x) = \omega^T \phi(x) + b \qquad (3)$$

where $\omega^T \epsilon R^d, b \epsilon R$. $\omega$ is called a weight vector and $b$ is called a bias. The optimal regression function is given by,

$$\min_{\omega, b, \xi_i, \xi_i^*} J = \frac{1}{2} \|\omega\|^2 + C \sum_{i=1}^{l} (\xi + \xi^*) \qquad (4)$$

subject to following,

$$y_i - \omega^T \phi(x_i) - b \le \epsilon + \xi_i \omega^T \phi(x_i) + b - y_i \le \epsilon + \xi_i^* \xi_i, \quad (5)$$
$$\xi_i^* \ge 0, i = 1, 2, ....d$$

where, $C \ge 0$, measures the tradeoff between complexity and minimizing loss, $\xi_i$ and $\xi_i^*$ are positive slack variables and $\epsilon$ is a fixed value of $\epsilon$ - insensitive loss function, which is defined as:

$$L^\epsilon(x, y, f) = |y - f(x)|^\epsilon = max(0, |y - f(x)| - \epsilon). \qquad (6)$$

The optimization problem in eq. (4) can be solved more easily in dual formation:

$$\max(-\frac{1}{2} \sum_{i,j=1}^{l} (\alpha_i - \alpha_i^*)(\alpha_j - \alpha_j^*) - \qquad (7)$$

$$\epsilon \sum_{i=1}^{l} (\alpha_i + \alpha_i^*) + \epsilon \sum_{i=1}^{l} Y_i (\alpha_i - \alpha_i^*))$$

subject to,

$$\sum_{i=1}^{l} (\alpha_i - \alpha_i^*) = 0, \alpha_i, \alpha_i^* \epsilon [0, C] \qquad (8)$$

where, $\alpha_i, \alpha_i^*$ are Lagrange coefficients and $K$ is termed as a kernel matrix. There are several possibilities for the choice of kernel function, including polynomial, sigmoid, and radial basis function (RBF). In this study, RBF is used to map the input data into a higher dimensional feature space, which is given by:

$$K(X_i, K_j) = \exp(-\gamma \|X_i - X_j\|^2) \qquad (9)$$

There are two parameters while using RBF kernels: kernel parameter $\gamma$ and penalty parameter $C$. The parameter selection is done using grid search method[1]. Once the optimal solution of eq. (7) has been found, the nonlinear regression function in original input space is given by:

$$f(x) = \sum_{i=1}^{l} (\alpha_i - \alpha_i^*) K(X_i, X_j) + b. \qquad (10)$$

For more detailed description refer to [22].

To learn the weighting parameters, we establish a validation dataset that comprises of particles from all classes,

---

[1] A grid search tries values of each parameter across the specified search range using geometric steps.

randomly chosen while ensuring no overlap with the training dataset. Features are computed and projected in each of the three subspaces. Similarity score for each particle is computed independently in each subspace against the corresponding training data matrix. Hence, for $m$ samples in the validation dataset and $n$ samples in the training dataset, the resulting similarity score is a vector of length $m \times n$. A similarity score matrix of size $(m \times n) \times 3$ is realized by considering the scores from each subspace. SVR is then used to compute the weighting parameters against the known ground-truth class labels for each sample in the validation dataset.

## 3. EXPERIMENTS AND RESULTS

To evaluate the merit of our proposed approach, we obtained urinary sediment samples from 45 patients. Each sample was imaged using a multispectral microscope under transmitted illumination. The microscope was calibrated according to the method described in [21] and 31 images were collected for each field of view ranging from 400-700nm in increments of 10nm. A single brightfield image was also collected for each field of view. A total of 452 images were collected. 60% of the images were randomly sampled to generate a training dataset. Approximately 25% of the remaining images were sampled to generate a validation dataset while the remaining 15% images were used to create a test dataset. Each dataset was sampled to ensure representation of all urine particles. Six distinct urinary particles, including red blood cells (RBC), white blood cells (WBC), uric acid, calcium oxalate, triple phosphate and hyaline, were manually identified and verified by two clinicians. Table 1 shows the distribution of these urinary particles.

Table 1: Class Distribution

| Uric Acid | Hyaline Cast | Triple Phosphate | Calcium Oxalate | RBC | WBC |
|---|---|---|---|---|---|
| 26 | 32 | 47 | 153 | 97 | 97 |

Next, individual particles were detected in each image using the segmentation algorithm described in section 2.1. A binary mask was generated for each of the segmented particle and its centroid used to place a bounding box to delineate the region of interest (ROI). Difference of Descriptors (DOD) was computed for every ROI to obtain the feature matrix as described in section 2.2, resulting in a matrix corresponding to the three datasets, training, validation, and testing. Each feature matrix was subject to projection into a 35 dimensional subspace using PCA, ISO, and NPE as explained in section 2.3.

For the training dataset, let the bases of the three space be $B_1, B_2, B_3$ and the respective projected spaces be $P_1, P_2, P_3$. The validation dataset is subject to projection using the bases $B_1, B_2, B_3$ for each of the three subspaces resulting in the projected spaces $V_1, V_2, V_3$, respectively. In case of particles from the training and validation datasets, each feature is associated with a class label from the set $\{1, 2, 3, 4, 5, 6\}$, corresponding to the particle type. The next step is to establish a discrimination criterion in each of the three subspaces and realize a weighted consensus that can be used for classification of the particles in the test dataset. Algorithm 3 details the steps of learning the decision function.

**Algorithm 3** Algorithm for learning the SVR parameters.

**for** $j = 1$ to 3 **do**
  **for** each validation row $i$ **do**
    **for** each training row $k$ **do**
      1. Compute the similarity score between $i^{th}$ validation row and $k^{th}$ training row.
    **end for**
    1. Store the similarity scores in column vectors.
  **end for**
  1. Concatenate all the similarity score vectors to form one similarity score vector.
**end for**
**for** each validation row $i$ **do**
  **for** each training row $k$ **do**
    **if** validation label $i == $ training label $k$ **then**
      1. Define label as 1.
    **else**
      2. Define label as 0.
    **end if**
  **end for**
  1. Concatenate all the label vectors to form one label vector.
**end for**
1. The three similarity vectors and label vector so obtained are used in support vector regression [5] as described in section 2.5 to obtain the weighting parameters for fusion.

The training stage results in the weighting parameters necessary for classification of new particles. Algorithm 4 details the steps for testing.

**Algorithm 4** Algorithm for testing of a new region of interest or particle.

1. Compute the descriptor for each pixel in the region of interest and project the feature vector into the three subspaces using the learned bases.
2. Compute the three similarity score vectors according to algorithm 2.
3. Arrange the similarity scores obtained as detailed in section 2.5 and using the weighting parameters obtained from algorithm 3, get the fused vector.
4. Search the fused vector to find the value closest to 1.
5. Obtain the corresponding class label of the entry to assign the particle to that class.

To quantify the performance of our approach, testing was subject to 50-fold cross-validation. Hence, we established a training, validation, and testing dataset 50 separate times based on random sampling from the original set of images. Each time, the performance of the algorithm was measured in terms of accuracy, precision, and specificity. Formally, these can be defined as:

1. Accuracy: Accuracy is the overall correctness of the model and is calculated as the sum of correct classifications divided by the total number of classifications.

$$Accuracy = \frac{tp + tn}{tp + tn + fn + fp}, \qquad (11)$$

where $tp$ and $tn$ are the numbers of true positive and true negative predictions for the considered class. $tp+$

$tn + fn + fp$ is the total number of examples of the considered class.

2. Specificity: Specificity corresponds to the true-negative rate.

$$Specificity = \frac{tn}{tn + fp}. \qquad (12)$$

3. Precision: Precision is a measure of the accuracy provided that a specific class has been predicted.

$$Precision = \frac{tp}{tp + fp}, \qquad (13)$$

4. Recall: Recall is a measure of true positive rate.

$$Precision = \frac{tp}{tp + fn}, \qquad (14)$$

The average result of 50 experiments is shown in figure 5 in the form of a confusion matrix.

| ACTUAL / PREDICTED | CAOX | HYAL | PHOS | RBC | URIC | WBC |
|---|---|---|---|---|---|---|
| CAOX | 19.4 | 0 | 0.3 | 0 | 0 | 0.2 |
| HYAL | 0.3 | 5 | 0 | 0.2 | 0.2 | 0 |
| PHOS | 0.3 | 0 | 5.6 | 0 | 0.6 | 0 |
| RBC | 0.2 | 0 | 0 | 13.8 | 0 | 0 |
| URIC | 0.3 | 0 | 0.2 | 0 | 2.8 | 0.2 |
| WBC | 0.5 | 0 | 0.9 | 0 | 0.4 | 13.6 |

Figure 5: Classification of urine particles with decision fusion for multispectral data. In the intersection of row i with column j, we have percentage of items belonging to class i that have been assigned to class j. Diagonal shows the percentage of correct classification for each class.

We also evaluated the merit of decision fusion using SVR. In this case, classification decisions were obtained in each subspace independently. A training dataset comprised of 75% of the images such that the number of each particle type present was representative of the probability of occurrence of that class. Rest of the images were used for testing. 1-nearest-neighbor classifier[1] was used for obtaining the class label. Table 2 gives the overall accuracy, false positive rate (FPR), and false negative rate (FNR) of all the classes based on individual subspace classification as well as by fusion using SVR. Fusion method shows an average accuracy boost of 4.7% over the individual subspace classification accuracy. In order to provide more insight into performance of our system, we calculated specificity and precision of each particle. Results are shown in table 3, table 4, and table 5 for specificity, precision, and recall, respectively.

In order to validate the significance of multispectral data for urine sediment classification, we evaluated the performance of classification based on features computed from the brightfield image. In this case, only the DAISY features were computed for each pixel in the ROI. Performance was measured by taking 75% of the images in each class for training and rest for testing with random sampling from each class. 1-nearest-neighbor classifier was used for classification. The

---

[1]To classify an observation, we find the most similar example in the training set by computing cosine distance and return the class of that example.

Table 2: Classification performance of urine particles based on fusion with SVR, PCA, ISO, and NPE using multispectral data.

|          | SVR   | PCA   | ISO   | NPE    |
|----------|-------|-------|-------|--------|
| Accuracy | 92.6% | 86.0% | 90.6% | 87.2%  |
| FPR      | 1.5%  | 2.8%  | 2.0%  | 2.7%   |
| FNR      | 10.3% | 16.9% | 14.9% | 14.72% |

Table 3: Specificity of classifying urine particles based on fusion with SVR, PCA, ISO, and NPE using multispectral data

|                  | SVR   | PCA   | ISO   | NPE   |
|------------------|-------|-------|-------|-------|
| Calcium Oxalate  | 98.9% | 97.3% | 96.4% | 91.9% |
| Hyaline          | 99.8% | 98.3% | 98.5% | 99.3% |
| Triple Phosphate | 98.5% | 95.5% | 98.6% | 97.2% |
| RBC              | 99.6% | 97.6% | 99.2% | 98.8% |
| Uric Acid        | 98.9% | 97.9% | 99.3% | 97.9% |
| WBC              | 96.5% | 96.5% | 96.2% | 98.8% |

average result of 50-fold cross-validation is shown in figure 6. Table 6 gives the overall accuracy, false positive rate (FPR),



Figure 6: Classification of urine particles with decision fusion for regular microscopic examination. In the intersection of row i with column j, we have percentage of items belonging to class i that have been assigned to class j. Diagonal shows the percentage of correct classification for each class.

and false negative rate (FNR) of all the classes based on individual subspace classification as well as by fusion using SVR. The results clearly shows the significance of multispectral data. Fusion method for multispectral data shows an accuracy boost of 11.0% over the brightfield data. Also, multispectral data provides significant improvement in FPR and FNR of the system in comparison to brightfield data. To further examine the benefit of multispectral data, we calculated specificity, precision, and recall of each particle classified using brightfield data. Results are shown in table 7, table 8, and table 9 for specificity, precision, and recall, respectively.

Table 8: Precision of classifying urine particles based on fusion with SVR, PCA, ISO, and NPE using brightfield data.

|                  | SVR   | PCA   | ISO   | NPE   |
|------------------|-------|-------|-------|-------|
| Calcium Oxalate  | 86.4% | 91.8% | 56.9% | 59.6% |
| Hyaline          | 93.0% | 100%  | 60.8% | 27.8% |
| Triple Phosphate | 87.2% | 90.7% | 30.4% | 34.7% |
| RBC              | 82.0% | 82.3% | 72.9% | 46.7% |
| Uric Acid        | 40.0% | 61.9% | 28.6% | 0%    |
| WBC              | 76.7% | 69.0% | 45.9% | 39.3% |

Table 4: Precision of classifying urine particles based on fusion with SVR, PCA, ISO, and NPE using multispectral data.

|                  | SVR   | PCA   | ISO    | NPE   |
|------------------|-------|-------|--------|-------|
| Calcium Oxalate  | 97.5% | 93.1% | 92.3%  | 81.9% |
| Hyaline          | 87.7% | 82.8% | 84.2%  | 92.0% |
| Triple Phosphate | 86.2% | 64.4% | 85.0%  | 77.1% |
| RBC              | 98.6% | 92.6% | 97.14% | 95.7% |
| Uric Acid        | 80.0% | 59.4% | 84.0%  | 67.5% |
| WBC              | 88.3% | 88.1% | 88.05% | 95.7% |

Table 5: Recall of classifying urine particles based on fusion with SVR, PCA, ISO, and NPE using multispectral data.

|                  | SVR   | PCA   | ISO   | NPE   |
|------------------|-------|-------|-------|-------|
| Calcium Oxalate  | 92.4% | 77.1% | 91.9% | 95.0% |
| Hyaline          | 100%  | 96.0% | 96.0% | 92.0% |
| Triple Phosphate | 80.0% | 67.1% | 72.9% | 72.0% |
| RBC              | 98.6% | 100%  | 97.1% | 92.4% |
| Uric Acid        | 70.0% | 63.3% | 52.5% | 73.0% |
| WBC              | 97.1% | 95.0% | 100%  | 82.7% |

Table 9: Recall of classifying urine particles based on fusion with SVR, PCA, ISO, and NPE using brightfield data.

|                  | SVR   | PCA   | ISO   | NPE   |
|------------------|-------|-------|-------|-------|
| Calcium Oxalate  | 90.5% | 80.4% | 72.9% | 41.4% |
| Hyaline          | 80.0% | 94.0% | 90.0% | 74.0% |
| Triple Phosphate | 58.6% | 55.7% | 40.0% | 17.1% |
| RBC              | 91.4% | 92.9% | 72.9% | 84.3% |
| Uric Acid        | 25.0% | 32.5% | 10.0% | 0.00% |
| WBC              | 87.1% | 97.1% | 20.0% | 17.1% |

## 4. CONCLUSION AND DISCUSSION

Microscopic analysis of urinary sediment particles is a challenging problem exasperated by variations in shape, size, and texture of individual particles in the presence of noisy backgrounds. In this paper, we have presented a novel method for urine particle classification based on the use of local descriptors coupled with regression based decision fusion. Specifically, DAISY descriptors have been used to capture the textural characteristics of each particle and subjected to dimensionality reduction across three linear subspaces to increase the diversity in decision making along with lowering the "curse of dimensionality". Classification in each subspace is based on computing a similarity score, which is then fused through support vector regression to obtain a final classification. Moreover, the presented approach is applied to both brightfield and multispectral data to ascertain the benefits of multispectral imaging for urine analysis. Urine particles analyzed included crystals, casts and blood cells.

We have tested our algorithm on a dataset of 452 images and the results obtained show an average classification accuracy of 92.6% for 6 classes of urinary particles. Compared to brightfield data, this represents an improvement of over 11.0%. Results show that the proposed algorithm and the use of multispectral information can significantly improve the classification performance and can aid in the process of identifying and differentiating various urine particles. This approach can easily be augmented to support additional features, such as those that may capture the morphometry of

Table 6: Classification performance for urine particles based on fusion with SVR, PCA, ISO, and NPE using brightfield data.

|          | SVR   | PCA   | ISO   | NPE   |
|----------|-------|-------|-------|-------|
| Accuracy | 81.6% | 82.1% | 55.4% | 42.8% |
| FPR      | 3.9%  | 3.8%  | 9.6%  | 11.8% |
| FNR      | 27.9% | 24.5% | 49.0% | 61.0% |

Table 7: Specificity of classifying urine particles based on fusion with SVR, PCA, ISO, and NPE using brightfield data.

|                  | SVR   | PCA   | ISO   | NPE   |
|------------------|-------|-------|-------|-------|
| Calcium Oxalate  | 93.2% | 96.6% | 73.6% | 86.6% |
| Hyaline          | 99.5% | 100%  | 95.1% | 84.0% |
| Triple Phosphate | 99.0% | 99.3% | 89.0% | 96.0% |
| RBC              | 94.6% | 94.5% | 92.5% | 73.5% |
| Uric Acid        | 97.6% | 98.7% | 98.4% | 96.4% |
| WBC              | 92.6% | 88.0% | 93.5% | 92.7% |

particles. Combination of morphological and local features can greatly influence the performance of classification. In addition, Improved segmentation of particles can also boost the classification system. These are consideration for our future work.

# 5. REFERENCES

[1] H. Bay, T. Tuytelaars, and L. V. Gool. Surf: Speeded up robust features. *9th European Conference on Computer Vision*, pages 404–417, 2006.

[2] D. Cai, X. He, and J. Han. Isometric projection. *In Proc. 2007 AAAI Conf. on Artificial Intelligence*, 2007.

[3] H. Cai, K. Mikolajczyk, and J. Matas. Learning linear discriminant projections for dimensionality reduction of image descriptors. *PAMI*, 99, 2010.

[4] D. Carlson and B. Statland. Automated urinalysis. *Clin Chem Lab Med*, 25(2):449–461, 1988.

[5] C.-C. Chang and C.-J. Lin. LIBSVM: a library for support vector machines. 2001.

[6] J. Dahmen, J. Hektor, R. Perrey, and H. Ney. Automatic classification of red blood cells using gaussian mixture densities. *Bildverarbeitung fur die Medizin*, pages 331–335, 2000.

[7] D. Donoho. High-dimensional data analysis: The curses and blessings of dimensionality. lecture delivered at the "mathematical challenges of the 21st century. *conference of The American Math. Society*, 2000.

[8] R. Fergus, P. Perona, and A. Zisserman. Object class recognition by unsupervised scale-invariant learning. *IEEE Computer Society Conference on Computer Vision and Pattern Recognition*, pages 264–271, 2003.

[9] R. Gonzalez and R. Woods. *Digital Image Processing Using MATLAB*. Publishing House of Electronics Industry, 2004.

[10] X. He, D. Cai, S. Yan, and H. Zhang. Neighborhood preserving embedding. *in Proc. IEEE Int. Conf. Computer Vision*, pages 1208–1213, 2005.

[11] I. Jolliffe. *Principal Component Analysis*. Springer-Verlag, 1986.

[12] Y. Ke and R. Sukthankar. Pca-sift: A more distinctive representation for local image descriptors. *CVPR*, pages 506–513, 2004.

[13] J. Kittler, I. C. Society, M. Hatef, R. P. W. Duin, and J. Matas. On combining classifiers. *IEEE Transactions on Pattern Analysis and Machine Intelligence*, 20:226–239, 1998.

[14] S. Lazebnik, C. Schmid, and J. Ponce. Beyond bags of features: Spatial pyramid matching for recognizing natural scene categories. *Conference on Computer Vision and Pattern Recognition*, 2006.

[15] D. Lowe. Distinctive image features from scale-invariant keypoints. *Int. J. Comput. Vis*, 60(2):91–110, 2004.

[16] Mei-Li, Shen, Dian-Ren, and Chen. Study on urinary sediments classification and identification techniques. *Proceedings of the SPIE*, 6027:341–346, 2006.

[17] Y. Murasaki, K. Tanigiichi, and Y. Murakami. Pattern recognition of urinary sediment images applying a fuzzy-neural network. *Trans. of IECE*, 76.

[18] A. Paranjape, K. Castleman, T. E. Milner, and H. R. III. Advanced imaging technique for automated classification of casts and crystals in urine. *SPIE*, 6424:64240X, 2007.

[19] M. Ranzato, P. Taylor, J. House, R. Flagan, Y. LeCun, and P. Perona. Automatic recognition of biological particles in microscopic images. *Pattern Recognition Letters 28*, 28:31–39, 2007.

[20] S. Shah, M. Schwartz, D. Mody, M. Scheiber-Pacht, and M. Amrikachi. The role of multispectral microscopy in differentiating benign and malignant thyroid nodules: a pilot study of 24 cases. *Proceedings of the Annual Meeting of the United States and Canadian Academy of Pathology*, 2008.

[21] S. Shah, J. Thigpen, F. Merchant, and K. Castleman. Photometric calibration for automated multispectral imaging of biological samples. *Proceedings of the 1st Workshop on Microscopic Image Analysis with applications in Biology (in conjunction with MICCAI, Copenhagen)*, pages 27–33, 2006.

[22] A. Smola and B. Schölkopf. *A tutorial on support vector regression*. Statistics and Computing, 2001.

[23] J. Szwed and C. Schaust. The importance of microscopic examination of the urinary sediment. *Am J Med Technol*, 48:141–143, 1982.

[24] E. Tola, V. Lepetit, and P. Fua. A fast local descriptor for dense matching. *CVPR*, pages 1–8, 2008.

[25] T. Tuytelaars and L. V. Gool. Wide baseline stereo matching based on local, affinely invariant regions. *In Proc. British Machine Vision Conf.*, pages 412–425, 2000.

[26] V. Uebele, S. Abe, and M. Lan. A neural-network-based fuzzy classifier. *IEEE Transactions on System, Man and Cybernetics*, 25(2):353–361, 1995.

[27] L. Zeng and Q.Wu. Comparison of three automated urinalysis systems - bayer clinitek atlas, roche urisys 2400 and arkray aution max for testing urine chemistry and detection of bacteriuria. *Lecture Notes in Computer Science*, 4222:734–741, 2006.